THE JOURNAL OF PHYSICAL CHEMISTRY C
A JOURNAL OF THE AMERICAN CHEMICAL SOCIETY

pubs.acs.org/JPCC

Article

Elucidating the Mn^{2+} Dopant Sites in Two-Dimensional Na−In Halide Perovskite

Priyesh Yadav, Deepika Gill, Swati Khurana, Raman Singh Lamba, Saswata Bhattacharya,* and Sameer Sapra*

Cite This: *J. Phys. Chem. C* 2023, 127, 3609−3618

Read Online

ACCESS | Metrics & More | Article Recommendations | Supporting Information

ABSTRACT: The layered hybrid double perovskites (LDPs) possess excellent stability and environmental friendliness, which makes them remarkable semiconducting materials. Contrary to significant advancements, the nonfluorescent nature at ambient temperature and pressure is still a major hurdle in this intriguing family. Here, we demonstrate doping of the transition metal cation Mn^{2+} in two-dimensional (2D) $(PEA)_4NaInCl_8$ (PEA = phenylethylamine) LDP, by a solution-processed crystallization method. This results in broadband emission at ambient conditions and initial contraction followed by expansion of host lattice on increasing dopant concentration. A higher dopant feed ratio in this wide band gap material leads to the absorption at 2.95 eV due to the $^6A_1$ (^6S) → $^4A_1$ (^4G) transitions on Mn^{2+} centers. First-principles calculations based on density functional theory (DFT) confirm that Mn^{2+} in substitutional sites results in lattice contraction while interstitial site Mn^{2+} doping leads to lattice expansion. The potential of Mn^{2+} to improve optical and magnetic properties of host lattice and a deeper understanding of distribution of Mn^{2+}dopant make these LDPs a promising material for emitters for solid-state lighting and magneto-optical applications.

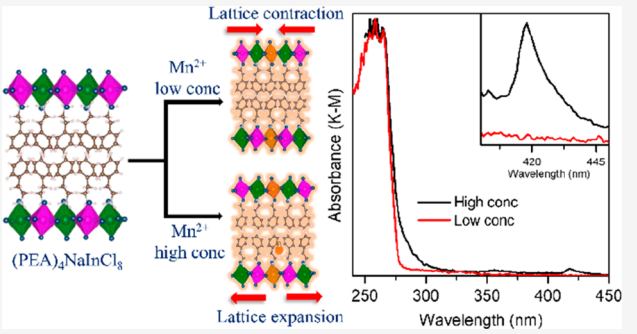

INTRODUCTION

Hybrid layered perovskites exhibit useful optoelectronic properties with some attractive features as compared to their 3D analogues.[1−3] They display significant ambient stability, greater chemical and structural diversity, ease of device fabrication, and excellent tunability of properties.[4,5] The discovery of hybrid layered double perovskite (LDP) is a recent advancement in this field.[6] These LDPs consist of monovalent and trivalent metals, arranged in a regular fashion forming 2D inorganic layer of perovskite with large organic amine cations separating the inorganic layers and balancing the charge. When monovalent ammonium cation separates the layers, Ruddlesden−Popper (RP) type structures are formed. Figure 1a depicts the RP phase with general formula $A'_4M^IM'^{III}X_8$ for n = 1 (where n is no. of inorganic slabs), where A′ is the monovalent ammonium cation, which separates the inorganic layers, formed by alternating corner sharing octahedra $[MX_6]^{5-}$and $[M'X_6]^{3-}$, respectively, while M^I = Na, Ag, or some monovalent transition metal ion, M'^{III} = Bi, In, Sb, or some trivalent transition metal ion, and X = Cl^-, Br^-, and I^-.[6−12]

Though LDPs are green alternatives of toxic Pb-based layered perovskites,[13] however, unlike lead-based layered perovskites, LDPs are nonemissive at ambient temperature and pressure.[7−11] The nonfluorescent nature of LDPs makes them unsuitable candidates for their application in the optoelectronic field, e.g., light-emitting diodes (LEDs), solid-state lighting (SSL), etc.[14] The reason for their nonfluorescent nature at ambient conditions is unclear yet and requires further research. Recent literature has delved into studying the emissive properties of these LDPs. Many previously reported LDPs are nonfluorescent at ambient conditions but emissive at low temperature or high pressure. $PA_4AgInBr_8$ (PA = propylammonium) displays broadband fluorescence emission only below 100 K.[7] $(BA)_4AgBiBr_8$ (BA = *n*-butyl amine) shows the band edge emission below 160 K, which is otherwise nonfluorescent at room temperature.[15] Zou et al. successfully demonstrated broadband white light emission from $(BA)_4AgBiBr_8$ at room temperature by applying very high pressure, intensifying the anisotropic deformation of elastic lattices and perturbs the detrapping of self-trapped excitons (STEs).[16] Our group has recently added a new emission feature at low temperature in $(BA)_4AgBiBr_8$ at 625 nm by doping Mn^{2+}, a transition metal cation.[15] Zhang et al. introduced broadband white light emission at room temper-

Received: December 5, 2022
Revised: January 26, 2023
Published: February 8, 2023

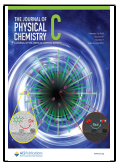

https://doi.org/10.1021/acs.jpcc.2c08506
J. Phys. Chem. C 2023, 127, 3609−3618

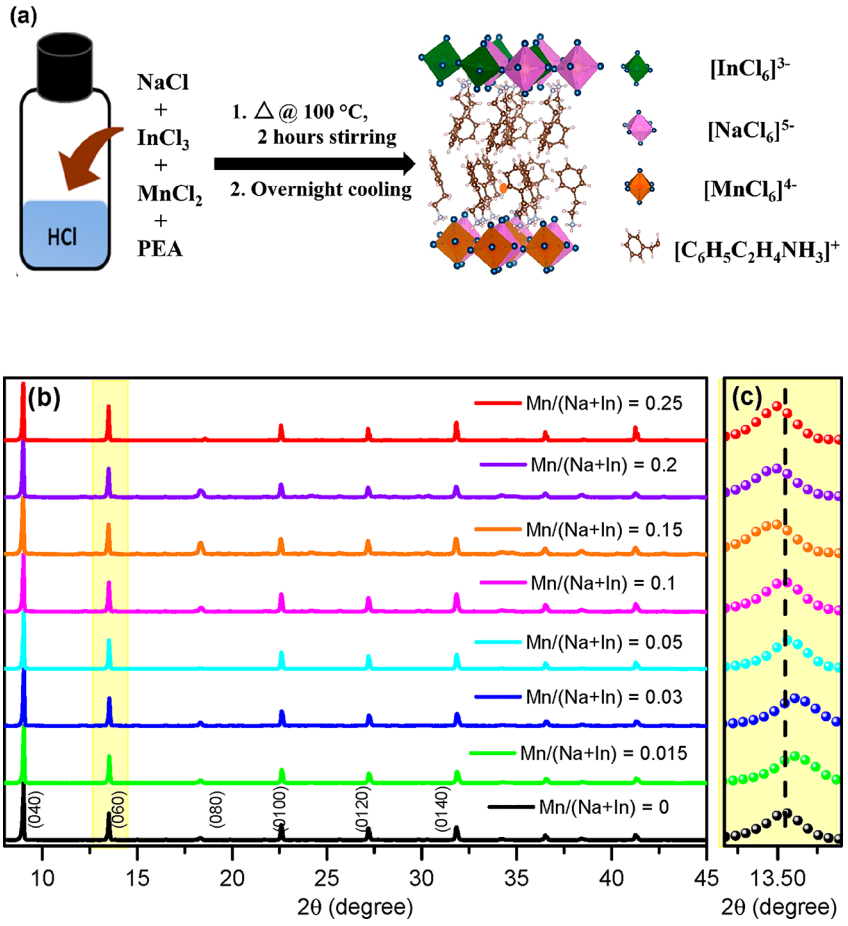

Figure 1. (a) Schematic showing synthesis methodology (left) for Mn^{2+} doped $(PEA)_4NaInCl_8$ along with the its schematic crystal structure (right); (b) PXRD patterns of Mn^{2+}-doped $(PEA)_4NaInCl_8$ with different Mn/(Na+In) nominal ratios; (c) magnified view of the (060) diffraction peak.

ature and pressure in $(PEA)_4NaInCl_8$ and $(PEA)_2CsNaInCl_7$ by doping it with Sb^{3+}, attributed to the STE emission in otherwise nonemissive materials.[12] Beside the work by Zhang et al., none of these studies focus on the fluorescence at ambient conditions, rendering these materials limited for optoelectronic applications.[14] These issues are currently motivating the material scientists to find a way in order to make these materials emissive at ambient conditions. Through the controllable doping of certain homo or heterovalent cations, new emission features can be added to these materials. The choices for the optically active dopant, for the wide band gap host semiconductors, have been mainly transition metals, such as Mn^{2+}.[17,18] Extensive research has been conducted on the incorporation and effects of Mn^{2+}, including the chemical and structural changes, spatial distribution of dopant, and energy transfer phenomenon of host to dopant resulting in a signature orange-red emission.[19−23] The sensitization mechanism of dopant from host is not yet clear; it could be from band edge to dopant ion or from the defect mediated energy transfer.[24−26]

Mn^{2+} incorporation into LDPs can possibly occur at two sites: substitution of the M-site mono/trivalent metal and occupation of interstices in the lattice. The incorporation route of dopant would affect the system differently, leading to changes in the lattice and electronic structure. The interstitial sites in the case of LDPs are provided by the free space in the region occupied by the organic chains. Lattice contraction/expansion is expected upon occupation of substitutional sites of semiconductor lattice by Mn^{2+}.[27,28] However, recent literature on the substitution of Pb^{2+} (ionic radii 1.19 Å)[29] by Mn^{2+} (ionic radii 0.83 Å)[29] in many inorganic and hybrid perovskite structures shows all types of lattice distortions, viz., contraction,[28,30−34] expansion,[33] and no change[27,35,36] in lattice through X-ray diffraction (XRD) measurements. The dopant incorporation type in these systems is not well understood. To better understand these anomalous observations, it would be quite appealing to study the spatial distribution of dopants inside the host lattice.

In this work, the structural and optical properties of Mn^{2+} doped lead-free LDP $(PEA)_4NaInCl_8$ were investigated systematically. We synthesized bulk Mn^{2+} doped $(PEA)_4NaInCl_8$ having a 2D lamellar architecture, by a solution-processed crystallization method based on slow cooling of concentrated solutions, with nominal Mn/(Na+In) feed ratios ranging from 0 to 0.25. Here, we found that Mn^{2+} doping could effectively improve the emission properties of $(PEA)_4NaInCl_8$. Furthermore, we observe expansion in the lattice at higher dopant concentrations. Density functional theory (DFT) calculations simulate that the observed expansion in this LDP lattice is due to the presence of Mn^{2+} dopants at interstitial sites, thereby supporting the results of our experiments. Based on experimental and theoretical results, we propose an apparent mechanism regarding the type of distribution of Mn^{2+} into the host $(PEA)_4NaInCl_8$ LDP lattice.

https://doi.org/10.1021/acs.jpcc.2c08506
J. Phys. Chem. C 2023, 127, 3609−3618

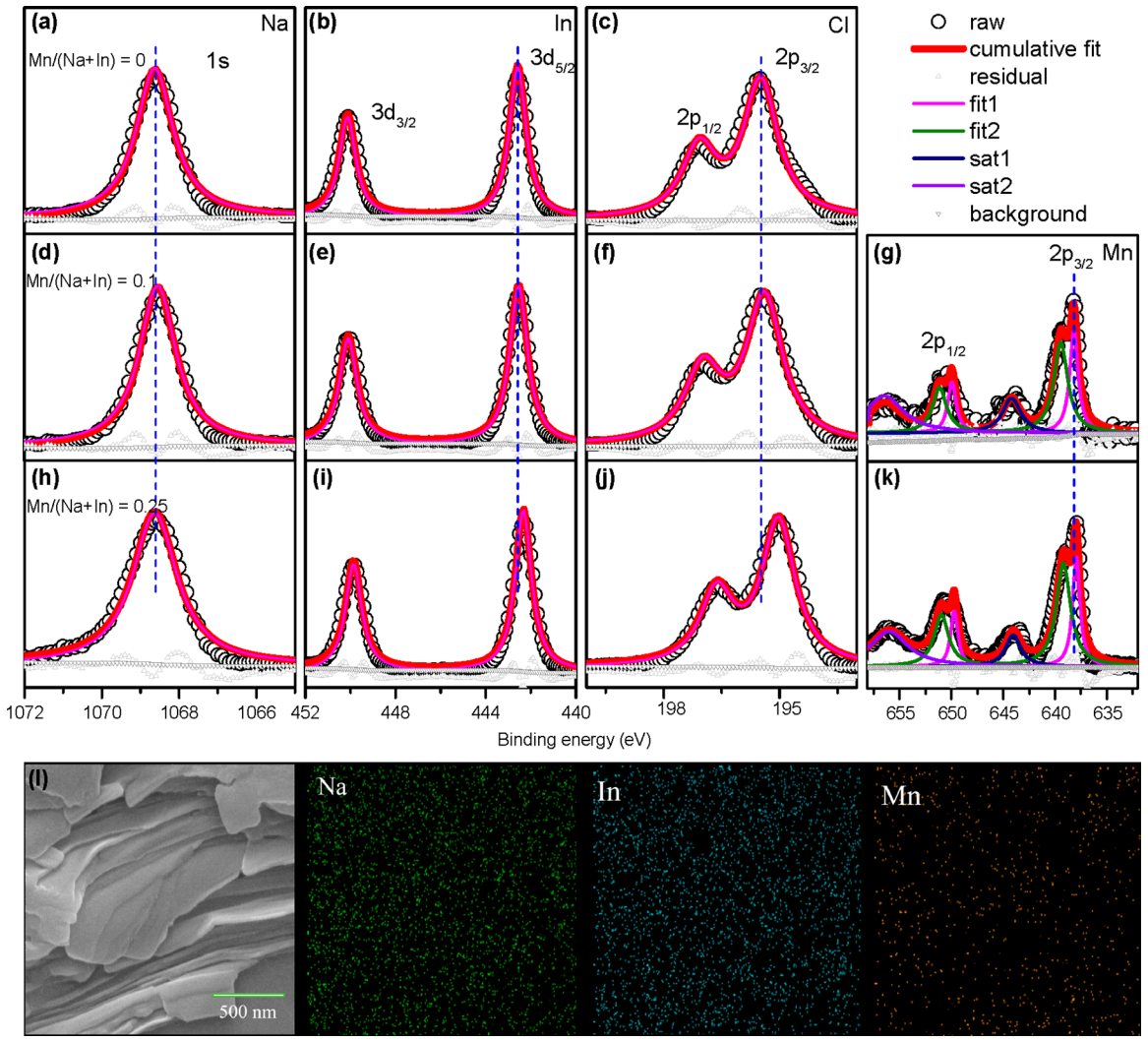

Figure 2. XPS core level spectra of (a–c) Na 1s, In 3d, and Cl 2p peaks of pure $(PEA)_4NaInCl_8$; (d–g and h–k) Na 1s, In 3d, Cl 2p, and Mn 2p peaks of samples with nominal doping Mn/(Na+In) = 0.1, and 0.25, respectively. (l) Field emission scanning electron microscopy (FESEM) image of $(PEA)_4NaInCl_8$ with nominal doping Mn/(Na+In) = 0.1 showing a layered morphology and elemental mapping showing the distribution of Na, In, and Mn corresponding to this image.

The observations of the optical and magnetic phenomena have been helpful for both magneto-optical applications and verifying the presence of the Mn^{2+} dopant in samples.[37−39] To the best of our knowledge, so far there is no report on heterovalent doping inside a LDP lattice, resulting in emission at ambient conditions and describing the distribution of dopants inside the host LDPs lattice. The finding of our work describes the behavior of optically active divalent cations doped into the LDP lattice, which can be potentially relevant in developing optoelectronic devices,[17,28,32] viz., LEDs for SSL,[14] and in spintronics.[37−39]

METHODS

Materials. $InCl_3$ (99.999% trace metals basis), NaCl (≥99.0%), $MnCl_2$ (≥99% trace metals basis), HCl (ACS reagent, 37%), and phenylethyl amine (PEA) (≥99%) were purchased from Sigma-Aldrich and used without further purification.

Synthesis of $(PEA)_4NaInCl_8$ 2D Layered Double Perovskite. All the synthesis experiments were carried out in air unless stated otherwise. Synthesis of $(PEA)_4NaInCl_8$ crystals was carried out by a solution-processed crystallization method based on the slow cooling of concentrated solutions.[12] For the synthesis of $(PEA)_4NaInCl_8$ crystals, we mixed 0.5 mmol of $InCl_3$, 0.5 mmol of NaCl, and 2.5 mmol of PEA solution in a 15 mL glass vial containing 5 mL of concentrated hydrochloric acid (HCl). The vial with these precursors was heated at 100 °C with constant stirring for 2 h, to ensure the complete solubility of all the precursors, resulting in a clear transparent solution. The hot clear solution was naturally cooled to room temperature, producing the plate-like white crystals of $(PEA)_4NaInCl_8$. These crystals were filtered and washed with conc. HCl in order to dissolve any precursor impurities (if any), and dried in a vacuum oven for 24 h. The crystals obtained thus were used for further characterization.

Synthesis of Mn^{2+} Doped $(PEA)_4NaInCl_8$ 2D Layered Double Perovskite. For doping Mn^{2+} ions, a stochiometric amount of $MnCl_2$ salt was added to the precursors while the rest of procedure remained exactly same, resulting in the white plate-like crystals of Mn^{2+} doped $(PEA)_4NaInCl_8$, with different amounts of Mn^{2+} dopants.

https://doi.org/10.1021/acs.jpcc.2c08506
J. Phys. Chem. C 2023, 127, 3609−3618

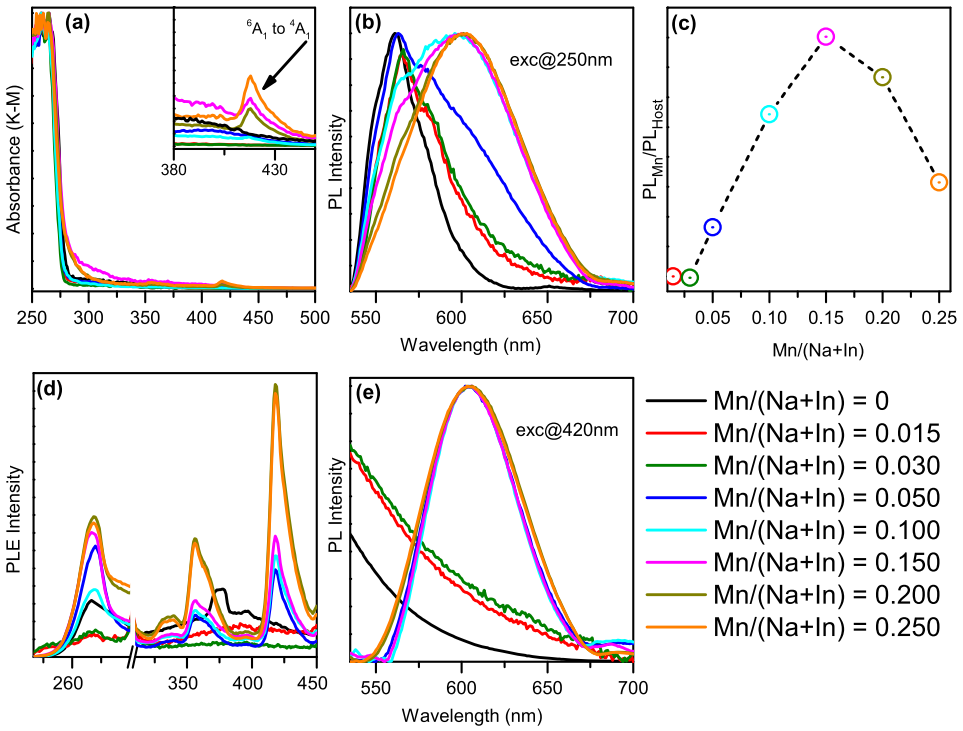

Figure 3. Optical measurements of pure and Mn^{2+} doped $(PEA)_4NaInCl_8$. (a) UV−visible pseudoabsorption spectra. The absorption spectra are converted from the measured diffused reflectance spectra by using Kubelka−Munk transformation,[51] Inset in (a) shows magnified view of UV−visible absorption spectra showing weak absorption feature at ∼420 nm for Mn^{2+} doped $(PEA)_4NaInCl_8$. (b) Steady-state photoluminescence (PL) spectra using 250 nm light radiation. (c) PL intensity ratio for dopant to host emission for Mn^{2+} doped $(PEA)_4NaInCl_8$. (d) PL excitation spectra using emission wavelength 562 nm for pure $(PEA)_4NaInCl_8$ and 600 nm for Mn^{2+} doped $(PEA)_4NaInCl_8$. (e) Steady-state PL spectra using 420 nm light radiation.

RESULT AND DISCUSSION

The synthesis of plate-like crystals of Mn^{2+} doped $(PEA)_4NaInCl_8$ LDP was performed by modifying the previously reported method.[12] In this approach, we mixed metal chloride salts and organic amine in concentrated hydrochloric acid (solvent) and heated to the desired temperature, until a clear solution was obtained. On cooling of this solution, plate-like crystals of Mn^{2+} doped $(PEA)_4NaInCl_8$ are obtained with different dopant concentrations. For reporting, nominal values of dopant concentration are used throughout the paper. More details of synthesis procedure are provided in the Methods section and are also shown in the scheme in Figure 1a. The schematic structure of Mn^{2+} doped $(PEA)_4NaInCl_8$ is shown in Figure 1a, containing alternating corner-sharing octahedra of $[InCl_6]^{3-}$ and $[NaCl_6]^{5-}$. Some octahedra of $[MnCl_6]^{4-}$ depict substitutional doping, while the PEA^+ constructs the organic layer that acts as a spacer cation connecting to the inorganic layers, with interchain van der Waals forces.[40] The purity of these as-prepared bulk undoped and doped crystalline materials was confirmed by powder X-ray diffraction (PXRD) patterns as shown in Figure 1b.

The PXRD patterns of both Mn^{2+} doped and pure $(PEA)_4NaInCl_8$ match well with the reference pattern of $(PEA)_4NaInCl_8$ (see Figure S1 in Supporting Information (SI) for enlarged pattern) with a monoclinic space group $P2_1/c$.[12] This rules out the formation of any undesired secondary phases on increasing the Mn/(Na + In) feed ratios. The cationic radius of Mn^{2+} (0.83 Å)[29] is closer to that of In^{3+} (0.80 Å)[29] compared to the larger Na^+ cation (1.02 Å).[29,41,42] Thus, there is a higher probability of Mn^{2+} replacing In^{3+}. However, the possibility of Mn^{2+} cation substituting the Na^+ cation or going to interstitial sites can also not be ignored as we deduce from the data in Figure 1c. The magnified view of the (060) reflection of PXRD patterns shown in Figure 1c shows that, upon doping with Mn^{2+} cation, the lattice of the host material initially contracts, and then upon increasing the dopant amount it gets expanded. The contraction could possibly arise due to the Mn^{2+} dopant occupying the larger Na^+ sites. As the radius of Mn^{2+} is close to that of In^{3+}, the substitution of In^{3+} with the Mn^{2+} is difficult to detect with PXRD. Further, with a higher feed ratio, the expansion of the lattice occurs, which we attribute to the occupation of interstitial sites. This type of expansion due to the presence of dopant ions at interstitial sites in perovskites is well-known in the literature.[43,44] Thus, by analyzing the PXRD patterns, we propose the presence of two types of Mn^{2+} sites inside the host LDP.

The presence of Mn^{2+} dopant cation at interstitial sites is further supported by inductively coupled plasmon−optically emission spectroscopy (ICP-OES) measurements, the results of which are shown in Table S1 in SI. ICP-OES results show that Mn^{2+} doping concentration inside the lattice is very high (up to 21%) at higher dopant concentration, which seems unrealistic in case of aliovalent substitutional doping of an ion. Presence of a higher dopant content leads us to infer that Mn^{2+} is not only going to substitutional sites but also resides at interstitial sites in the lattice.[43−45]

To get a deeper insight into the distribution/environment of Mn^{2+} ions, the chemical composition, and the valence state of the elements of these undoped and Mn^{2+} doped perovskites, we used X-ray photoelectron spectroscopy (XPS). We show

https://doi.org/10.1021/acs.jpcc.2c08506
J. Phys. Chem. C 2023, 127, 3609−3618

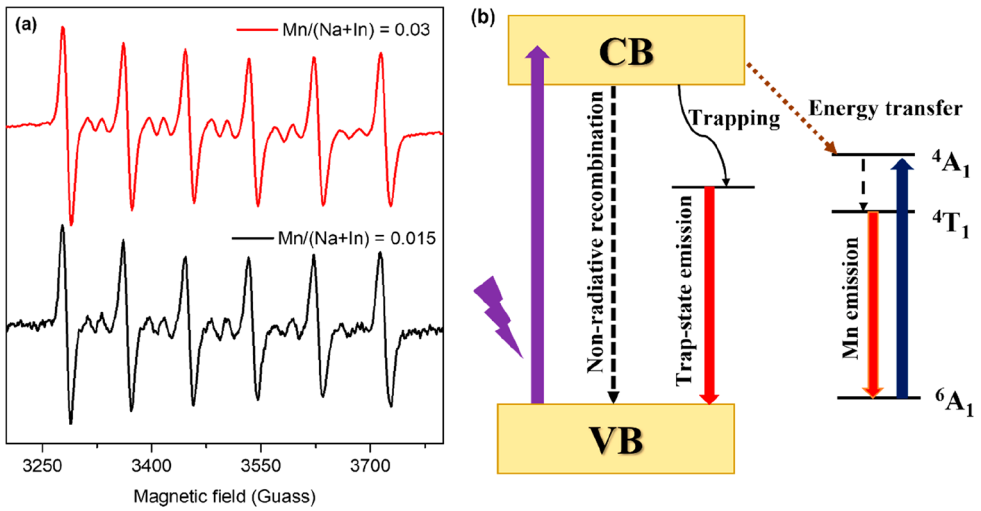

Figure 4. (a) Room-temperature X-band EPR spectra of Mn^{2+} doped $(PEA)_4NaInCl_8$, with Mn/(Na + In) ratio 0.015 (black), and 0.03 (red), showing characteristic 6-fold hyperfine coupling pattern of high-spin Mn^{2+}. (b) Scheme showing simplified view of relaxation pathways of excitons in Mn^{2+} doped $(PEA)_4NaInCl_8$.

the high resolution XPS core level spectra of Na 1s, In 3d, Cl 2p, and Mn 2p orbitals of pure material and with dopant concentrations 0.10, and 0.25 in Figure 2a–k. The analysis of the XPS spectra is fitted with pseudo-Voigt functions using a least-squares error fitting method with the minimum number of peaks needed to represent the spectra. Figure 2g and k shows peaks for Mn $2p_{3/2}$ and its corresponding spin–orbit coupling peak for $2p_{1/2}$, separated by 11.8 eV, confirming the +2 valence state of Mn.[46−48] Also, Mn^{2+} cations possess two types of chemical environments, assigned to the Mn^{2+} dopant at substitutional sites (at higher binding energy) and at interstitial sites (at lower binding energy), since the interstitial site ions are not too strongly bound. The satellite peaks are seen at 644 and 656 eV. In addition to this, the binding energies of Na 1s, In 3d, and Cl 2p for doped $(PEA)_4NaInCl_8$ decrease slightly compared to those of pure $(PEA)_4NaInCl_8$, inferring that the incorporation of Mn^{2+} in the lattice affects the chemical environment of all the species present in the system, i.e., Na^+, In^{3+}, and Cl^-.[44,49,50] To investigate the morphological and local chemical composition of undoped and doped $(PEA)_4NaInCl_8$, we performed field emission scanning electron microscopy-energy dispersive spectroscopy (FESEM-EDS). Figure 2l (for more images, see Figure S2) shows the layered architecture of $(PEA)_4NaInCl_8$:Mn^{2+}, similar to the undoped $(PEA)_4NaInCl_8$, indicating that doping of Mn^{2+} does not affect the morphology of the material. The elemental mapping corresponding to this image shown in Figure 2l confirms the spatial distribution of Na, In, and Mn throughout the structure.

The optical properties, including UV–vis absorption spectra, emission spectra, and excitation spectra, of undoped and doped materials were investigated systematically to understand the essential photophysical processes. UV–vis diffuse reflectance data was transformed using the Kubelka–Munk function to pseudoabsorbance.[51] As shown in Figure 3a, the strong increase in absorption was observed only below ∼280 nm, attributed to the interband transition of the organic layers.[12] Apart from this band edge absorption, there is weak background absorption at lower energies assigned to interband transitions of the inorganic layers.[12] The band gap, E_g, calculated from the Tauc plot (Figure S3), comes out to be 4.50 eV, which is similar to the reported value for this material.[12] Similar to the undoped $(PEA)_4NaInCl_8$, the strong absorption of Mn^{2+} doped samples occurs below ∼280 nm, along with an additional sharp peak at ∼420 nm (see inset to Figure 3a) for higher dopant concentrations (above dopant ratio 0.05), which is attributed to the d–d transition of Mn^{2+} ions from the ground state $^6A_1$ (^6S) to the excited state $^4A_1$ (^4G).[52] Figure 3b shows the steady-state photoluminescence (PL) spectra of undoped and doped materials excited with 250 nm light radiation. The undoped material exhibits weak PL emission centered at 562 nm, attributed to the trap states of the host.[53,54] On the other hand, for Mn^{2+} doped LDPs, an additional band is observed at 600 nm attributed to the $^4T_1$ to $^6A_1$ transition of octahedrally coordinated Mn^{2+} dopants.[17,19−23,27,28,30,55] PL emission spectra were fitted using Gaussian functions; the fits are shown in Figure S4. As estimated from the fits, the PL intensity ratio of Mn^{2+} to host emission, shown in Figure 3c, increases up to a dopant concentration of 0.15 due to the increasing probability of energy transfer from host to dopant ions. With a further increase in dopant amount, the number of interacting pairs of Mn^{2+} increases, leading to concentration quenching, which explains the decrease in dopant PL at higher concentrations.[56−58] Even though a reduced PL intensity is observed, the trap state emission of the host still exists at higher dopant concentration, implying the possibility of distinct energy transfer between the two PL bands. To differentiate their emergence, we measured the photoluminescence excitation (PLE) spectra for the emission at 562 nm for undoped and at 600 nm for Mn^{2+} doped samples. As shown in Figure 3d, the PLE spectra of doped materials resemble those of the undoped LDP, along with additional peaks at 420, 355, and 335 nm for higher dopant concentrations, indicating the different absorption contribution of Mn^{2+} d–d transitions compared to that of trap state emission. The additional peaks at 420, 355, and 335 nm for higher dopant concentrations in the PLE spectra are attributed to the spin-forbidden electronic transitions of Mn^{2+} ions from the ground state $^6A_1$ (^6S) to excited states $^4A_1$ (^4G), ^4E (^4D), and $^4T_1$ (^4P), respectively.[52,59,60] Eventually, PL spectra were collected at 420 nm excitation, displaying the pure Mn^{2+} emission with narrow peak

https://doi.org/10.1021/acs.jpcc.2c08506
J. Phys. Chem. C 2023, 127, 3609−3618

width as shown in Figure 3e.[17,19−23,27,28,30,55] It has been suggested that the appearance of the d−d transitions in the absorption spectra (inset to Figure 3a) and the emission corresponding to their excitation at 420 nm indicates the formation of Mn^{2+} pairs in the host lattice at higher dopant concentrations.[15,61−65] The Mn^{2+} d−d transitions are forbidden in octahedral coordination and hence rarely observed, but the magnetic coupling between Mn^{2+} pairs relaxes the selection rules.[56,57,61,66−69] From the PLE spectra, it is clear that Mn^{2+} emission is sensitized by the energy transfer from the $(PEA)_4NaInCl_8$ host lattice along with direct excitation of d-electrons of Mn^{2+} dopant ions. When the host material absorbs some suitable photon energy, electron−hole pairs are created within the lattice which migrate through the lattice until they are trapped by Mn^{2+} energy states where they recombine to emit at 600 nm.[56,70−75]

To further confirm the presence of Mn^{2+} dopant and their distribution inside $(PEA)_4NaInCl_8$ lattice, we perform the EPR measurement of doped materials. EPR spectroscopy is the method of choice for determining the chemical environment of Mn^{2+} ions within the host matrix.[76−78] As shown in Figure 4a, the room-temperature X-band EPR spectra of the 0.015 and 0.03 samples (see Figure S5 for EPR data of all the samples) displayed the characteristic sextet pattern due to hyperfine coupling of the electronic spin states, with the nuclear spin of isolated Mn^{2+} ions, with the g-factor of 2.0047 and a hyperfine constant A of 8.4 mT, which confirms the incorporation of Mn^{2+} cations into the LDP structure.[23,71] Higher Mn^{2+} doping leads to merging of the EPR signal into a single broad spectrum, implying the formation of Mn^{2+} cluster due to exchange interaction between magnetically coupled Mn^{2+} pairs.[15,61−68,79−81] This also explains the appearance of the 420 nm absorption peak at higher Mn^{2+} concentrations as discussed above.

Figure 4b summarizes the various processes and pathways involved in the de-excitation in these Mn^{2+} doped LDPs based on the above discussion. From this scheme, it can be seen that electrons from the conduction band can nonradiatively recombine with the hole in the valence band. Besides this, there are a couple of other possibilities: electrons get trapped into the defect states leading to emission at 562 nm by radiative recombination of charge, along with this, they can get trapped in Mn^{2+} energy states resulting in emission centered at 600 nm. There is direct excitation of Mn^{2+} d-electrons from the ground state ($^6A_1$) to the excited state, which relaxes back to the $^4T_1$ state nonradiatively where they finally relax to $^6A_1$ ground state giving relatively narrower pure Mn^{2+} emission, as shown in Figure 3e. A comprehensive study of energy transfer kinetics for Mn^{2+} doped LDPs is not available yet and requires further understanding.

The shift in PXRD patterns, XPS spectra of undoped and $(PEA)_4NaInCl_8$: Mn^{2+}, EPR spectra, and elemental and compositional analysis using ICP-OES and FESEM-EDS validate the successful incorporation of Mn^{2+} dopant, which occupies the substitutional as well as interstitial sites throughout the perovskite lattice. To gain more insights at the atomistic level on how the dopant distribution affects the lattice, we performed the DFT calculations to understand which dopant configuration leads to the lattice contraction or expansion. First lattice constants are obtained for the pristine, Mn^{2+} substitutionally doped, and Mn^{2+} interstitially doped 2D $(PEA)_4NaInCl_8$ configurations. The optimized lattice constants of monoclinic 2D $(PEA)_4NaInCl_8$ and Mn^{2+} doped configurations are given in Table 1.

Table 1. Lattice Parameters of Pristine and Mn^{2+} Doped Configurations, with Respective Change in the Lattice Parameters with Respect to Pristine

configuration	a (Å)	b (Å)	c (Å)	Δa %	Δb %	Δc %
$(PEA)_4NaInCl_8$	6.59	38.09	6.48	0	0	0
substitutionally doped system	6.56	37.98	6.47	−0.46	−0.29	−0.15
interstitially doped system	6.82	38.21	6.77	+3.49	+0.32	+4.48

Substitutional site (In and Na) doping by Mn^{2+} depicted in Figure 5a results in an overall lattice contraction as seen from Table 1. On the other hand, for Mn^{2+} interstitially doped perovskite, the Mn^{2+} ion resides between two benzene rings, bounded with H and C atoms of two benzene rings close to the octahedra. Pushing them apart from each other causes expansion in the lattice as shown in Figure 5b and Table 1. The optimized DFT model for pristine LDP, its band structure, and partial density of states (pDOS) are provided in Figure S6.

In the undoped system, the conduction band minimum (CBM) is contributed by the hybridized orbitals of In 6s and Cl 3p. Here, the 6s orbital of In is strongly hybridized with the 3p orbital of Cl, not with other orbitals. Hence, we observe a single band at CBM, whereas other dispersive conduction bands are slightly higher in energy. In the valence band maximum (VBM), the maximum contribution is from Cl 3p and C 2p orbitals. From the band structure, the VBM and CBM both lie at the G point with a band gap estimated to be 3.5 eV, which is not in agreement with the experimental value of 4.5 eV. Note that we have done all DFT calculations with the Perdew−Burke−Ernzerhof (PBE) functional, which underestimates the band gap due to the self-interaction error of a many-electron system. To overcome this problem, the advanced hybrid exchange−correlation (ε_{xc}) functional, viz., HSE06 or GW becomes essential.[82,83] As our unit cell consists of 188 atoms, utilizing HSE06 or GW is computationally very expensive and beyond our scope. However, the inferences derived from the present calculations should be qualitatively correct.

The band structure and pDOS for substitutionally and interstitially doped configurations are shown in Figure 5b,c and e,f, respectively. In the substitutionally doped system, the VBM is contributed by the C 2p orbital and CBM is contributed by the C 2p, In 5s, Cl 3p orbitals. A slight increase (∼0.02 eV) in the band gap of the dispersive bands is observed for the case of the substitutionally doped system. Whereas in the interstitially doped system, the VBM is contributed by the C 2p and Mn 3d orbitals and the CBM is contributed by C the 2p, In 5s, Cl 3p, and Mn 3d orbitals. Midgap states are introduced by the impurity, doping Mn^{2+} either substitutionally or interstitially. For the substitutionally doped system, there are two spin-up and two spin-down midgap bands. The lowest spin-up band lies 0.54 eV above the VBM. Two spin-down bands lie 0.81 eV below the CBM. As it is seen from the pDOS that these midgap bands are contributed by the Mn^{2+} 3d orbitals and bonded Cl 3p orbitals, here we expect a Mn^{2+} d−d transition from the spin-up bands above the VBM to spin-down bands below the CBM. In the interstitially doped system, from the

https://doi.org/10.1021/acs.jpcc.2c08506
J. Phys. Chem. C 2023, 127, 3609−3618

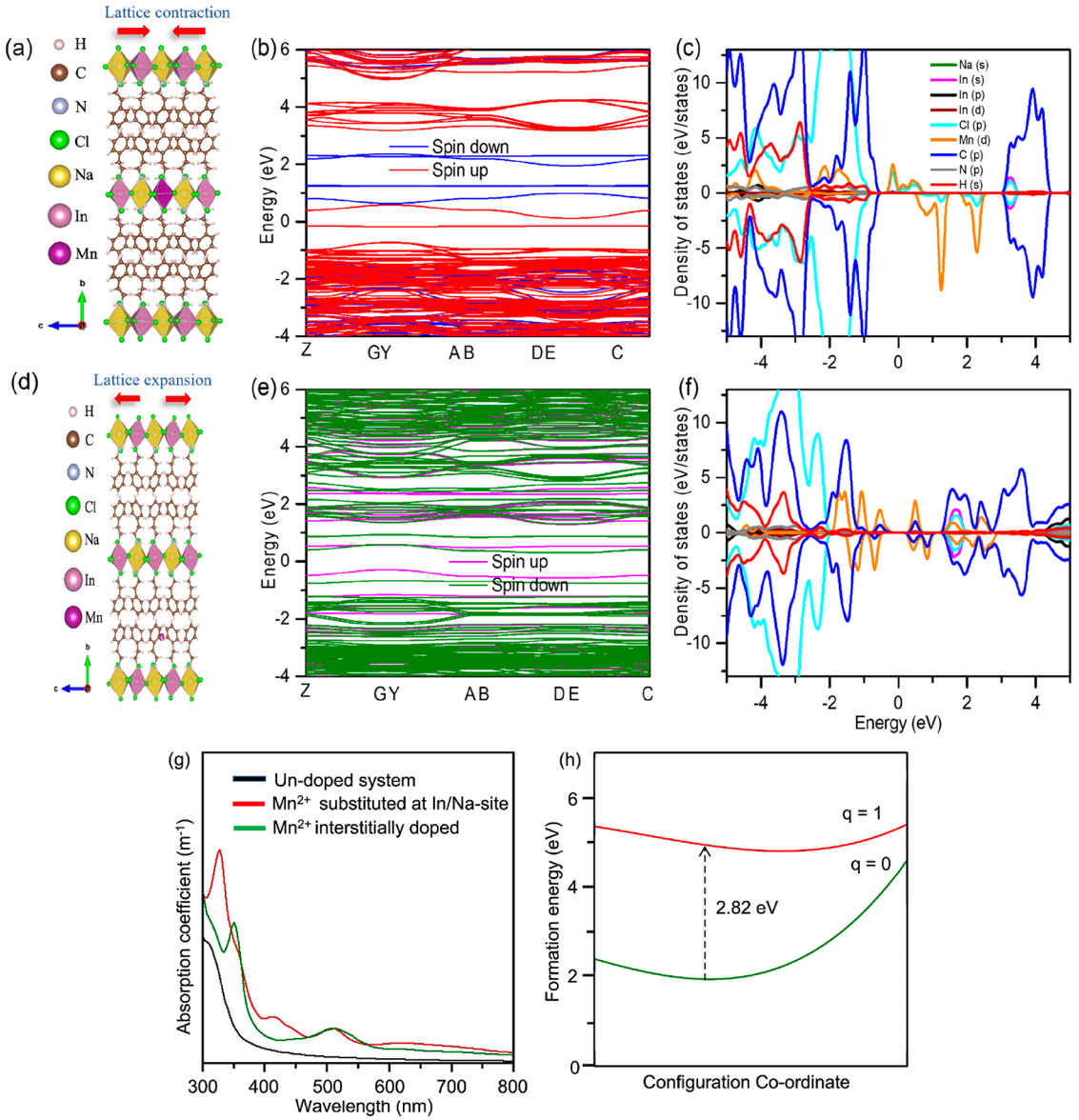

Figure 5. Single Mn^{2+} substitutionally doped at the Na or In site of 2D RP $(PEA)_4NaInCl_8$ (a) optimized crystal structure of the unit cell, (b) band structure, and (c) partial density of states (pDOS). Single Mn^{2+} interstitially doped 2D RP $(PEA)_4NaInCl_8$ (d) optimized crystal structure of unit cell, (e) band structure, and (f) pDOS. (g) Variation of absorption coefficient with the wavelength for undoped/doped $(PEA)_4NaInCl_8$. (h) Configuration coordinate (CC) diagrams for single Mn^{2+} substitutionally doped at In-site of 2D RP $(PEA)_4NaInCl_8$ as a function of the displacement of atoms, the formation energies in two different charge states; i.e., $q = 0$ and $q = 1$ are plotted.

band structure and pDOS, we observe three spin-up and three spin-down midgap bands, where two spin-up and one spin-down bands lie near the VBM. One spin-up and two spin-down bands lie near the CBM. Mn^{2+} d−d transitions from the middle gap spin-up/spin-down bands near the VBM to spin-down/spin-up bands near the CBM in addition to band gap transition are expected.

Further, we have also plotted absorption spectrum using the DFT approach by calculating dielectric coefficients for pristine and Mn^{2+} doped configurations. From Figure 5g, we can see that the absorption peak from the band gap transition is slightly red-shifted in the case of substitutionally doped Mn^{2+} and even more red-shifted in the case of interstitially doped Mn^{2+}. In the case of the Mn^{2+} doped configuration, the absorption peak at 420 nm corresponds to the Mn^{2+} d−d transition, from $^6A_1$ (^6S) to $^4A_1$ (^4G), which is absent in the case of pristine LDPs. Notably, as we have used the PBE functional, we have manually shifted the energy so that the absorption peak of pristine coincides with that of experimental.

Lastly, to capture the optical transition for the Mn^{2+} substituted at the In site, we have also plotted the configuration coordinate (CC) diagram.[84] The CC diagram represents the variation in the energy of electronic potential surface or levels with the nuclear displacements. This description considers only one vibrational coordinate, viz., configuration coordinate. Such diagrams aim to present the relative positions or crossing of different energy levels in detail along various geometries (with particular charge state). As Mn^{2+} substituted at In-site is a cation, hence we have shown optical transition from q = 0 state to q = 1 state (see Figure 5h). Here, absorption peak occurs at 2.82 eV i.e, in agreement with the experimental value.

https://doi.org/10.1021/acs.jpcc.2c08506
J. Phys. Chem. C 2023, 127, 3609−3618

CONCLUSION

In summary, here we have shown that emission of $(PEA)_4NaInCl_8$ improved greatly at ambient conditions on doping it with Mn^{2+} cations, attributed to the spin-forbidden $^4T_1$ to $^6A_1$ transition of Mn^{2+} d orbitals, which gives an emission centered at 600 nm. The shift in the PXRD pattern and XPS spectra of pure and doped materials confirms the presence of Mn^{2+} dopant into both the substitutional as well as interstitial sites of the $(PEA)_4NaInCl_8$ lattice. The excitation by 420 nm light radiation for higher dopant concentrations manifests the presence of a magnetic interaction between Mn^{2+} pairs at interstitial sites, which is further confirmed by the merging of the sextet into a single broad peak with an increase in dopant amount in the EPR spectra. Both our experimental and theoretical results suggest that Mn^{2+} dopants are present at substitutional as well as at interstitial sites, causing the expansion of the lattice. The extensive understanding of the distribution of Mn^{2+} in the lattice and changes in the lattice structure by the Mn^{2+} dopant and its ability to improve the photoluminescence and magnetic properties of host lattice will make these LDPs promising candidates for optoelectronic and spintronics applications.

ASSOCIATED CONTENT

Supporting Information

The Supporting Information is available free of charge at https://pubs.acs.org/doi/10.1021/acs.jpcc.2c08506.

PXRD pattern, FESEM images and elemental mapping, optical characterization, EPR studies, theoretical calculations (PDF)

AUTHOR INFORMATION

Corresponding Authors

Sameer Sapra − *Department of Chemistry, Indian Institute of Technology Delhi, New Delhi 110016, India;* orcid.org/0000-0002-1778-2884; Email: sapra@chemistry.iitd.ac.in

Saswata Bhattacharya − *Department of Physics, Indian Institute of Technology Delhi, New Delhi 110016, India;* orcid.org/0000-0002-4145-4899; Email: saswata@physics.iitd.ac.in

Authors

Priyesh Yadav − *Department of Chemistry, Indian Institute of Technology Delhi, New Delhi 110016, India;* orcid.org/0000-0003-0066-0116

Deepika Gill − *Department of Physics, Indian Institute of Technology Delhi, New Delhi 110016, India;* orcid.org/0000-0003-2299-1063

Swati Khurana − *Department of Chemistry, Indian Institute of Technology Delhi, New Delhi 110016, India;* orcid.org/0000-0002-1607-216X

Raman Singh Lamba − *Department of Chemistry, Indian Institute of Technology Delhi, New Delhi 110016, India*

Complete contact information is available at: https://pubs.acs.org/10.1021/acs.jpcc.2c08506

Notes

The authors declare no competing financial interest.

ACKNOWLEDGMENTS

PY acknowledges CSIR, India, for the senior research fellowship [Grant No. 09/086(1333)/2018-EMR-I], DG acknowledges UGC, India, for the senior research fellowship [grant no.: 1268/ (CSIR-UGC NET JUNE 2018)], SK is thankful to IIT Delhi for SRF fellowship and RSL is thankful to CSIR, India for the SRF [Grant No. 09/086(1307)/2018-EMR-I]. SS acknowledges Central Research Facility (CRF), IIT Delhi for using FESEM-EDS and EPR facility, and SERB Grant No. CRG/2019/000935 for partial financial assistance, SB acknowledges financial support from SERB under a core research grant (grant no. CRG/2019/000647) to set up his High Performance Computing (HPC) facility "Veena" at IIT Delhi for computational resources. We acknowledge the High Performance Computing (HPC) facility at IIT Delhi for computational resources.

REFERENCES

(1) Chakrabarty, A.; Satija, S.; Gangwar, U.; Sapra, S. Precursor-Mediated Synthesis of Shape-Controlled Colloidal $CsPbBr_3$ Perovskite Nanocrystals and Their Nanofiber-Directed Self-Assembly. *Chem. Mater.* **2020**, *32*, 721−733.

(2) Hassan, M. S.; Basera, P.; Bera, S.; Mittal, M.; Ray, S. K.; Bhattacharya, S.; Sapra, S. Enhanced Photocurrent Owing to Shuttling of Charge Carriers across 4-Aminothiophenol-Functionalized $MoSe_2$ − $CsPbBr_3$ Nanohybrids. *ACS Appl. Mater. Interfaces* **2020**, *12*, 7317−7325.

(3) Khurana, S.; Hassan, M. S.; Yadav, P.; Ghosh, D.; Sapra, S. Impact of Bifunctional Ligands on Charge Transfer Kinetics in $CsPbBr_3$ − CdSe/CdS/ZnS Nanohybrids. *J. Phys. Chem. Lett.* **2022**, *13*, 2591−2599.

(4) Cao, D. H.; Stoumpos, C. C.; Farha, O. K.; Hupp, J. T.; Kanatzidis, M. G. 2D Homologous Perovskites as Light-Absorbing Materials for Solar Cell Applications. *J. Am. Chem. Soc.* **2015**, *137*, 7843−7850.

(5) Smith, I. C.; Hoke, E. T.; Solis-Ibarra, D.; McGehee, M. D.; Karunadasa, H. I. A Layered Hybrid Perovskite Solar-Cell Absorber with Enhanced Moisture Stability. *Angew. Chemie - Int. Ed.* **2014**, *53*, 11232−11235.

(6) Evans, H. A.; Mao, L.; Seshadri, R.; Cheetham, A. K. Layered Double Perovskites. *Annu. Rev. Mater. Res.* **2021**, *51*, 351−380.

(7) Mao, L.; Teicher, S. M. L.; Stoumpos, C. C.; Kennard, R. M.; Decrescent, R. A.; Wu, G.; Schuller, J. A.; Chabinyc, M. L.; Cheetham, A. K.; Seshadri, R. Chemical and Structural Diversity of Hybrid Layered Double Perovskite Halides. *J. Am. Chem. Soc.* **2019**, *141*, 19099−19109.

(8) McClure, E. T.; McCormick, A. P.; Woodward, P. M. Four Lead-Free Layered Double Perovskites with the n = 1 Ruddlesden-Popper Structure. *Inorg. Chem.* **2020**, *59*, 6010−6017.

(9) Wolf, N. R.; Connor, B. A.; Slavney, A. H.; Karunadasa, H. I. Doubling the Stakes: The Promise of Halide Double Perovskites. *Angew. Chemie - Int. Ed.* **2021**, *60*, 16264−16278.

(10) Connor, B. A.; Biega, R.-I.; Leppert, L.; Karunadasa, H. I. Dimensional Reduction of the Small-Bandgap Double Perovskite $Cs_2AgTlBr_6$. *Chem. Sci.* **2020**, *11*, 7708−7715.

(11) Vargas, B.; RodrÍguez-López, G.; Solis-Ibarra, D. The Emergence of Halide Layered Double Perovskites. *ACS Energy Lett.* **2020**, *5*, 3591−3608.

(12) Zhang, Y.; Liu, X.; Sun, H.; Zhang, J.; Gao, X.; Yang, C.; Li, Q.; et al. Strong Self-Trapped Exciton Emissions in Two-Dimensional Na-In Halide Perovskites Triggered by Antimony Doping. *Angew. Chemie - Int. Ed.* **2021**, *133*, 7665−7670.

(13) Swarnkar, A.; Ravi, V. K.; Nag, A. Beyond Colloidal Cesium Lead Halide Perovskite Nanocrystals: Analogous Metal Halides and Doping. *ACS Energy Lett.* **2017**, *2*, 1089−1098.

(14) Sun, Y.; Giebink, N. C.; Kanno, H.; Ma, B.; Thompson, M. E.; Forrest, S. R. Management of Singlet and Triplet Excitons for Efficient White Organic Light-Emitting Devices. *Nature* **2006**, *440*, 908−912.

(15) Yadav, P.; Khurana, S.; Sapra, S. Doping Mn^{2+} in Hybrid Ruddlesden − Popper Phase of Layered Double Perovskite. *Nanotecnology* **2022**, *33*, 415706.
(16) Fang, A. Y.; Zhang, L.; Wu, L.; Yan, J.; Wang, K.; Mao, W. L.; Zou, B. Pressure-Induced Emission (PIE) and Phase Transition of a Two-dimensional Halide Double Perovskite $(BA)_4AgBiBr_8$ (BA = $CH_3(CH_2)_3NH_3^+$). *Angew. Chemie - Int. Ed.* **2019**, *58*, 15249−15253.
(17) Pradhan, N. Mn-Doped Semiconductor Nanocrystals: 25 Years and Beyond. *J. Phys. Chem. Lett.* **2019**, *10*, 2574−2577.
(18) Ohno, H. Making Nonmagnetic Semiconductors Ferromagnetic. *Science.* **1998**, *281*, 951−956.
(19) Yuan, X.; Ji, S.; De Siena, M. C.; Fei, L.; Zhao, Z.; Wang, Y.; Li, H.; Zhao, J.; Gamelin, D. R. Photoluminescence Temperature Dependence, Dynamics, and Quantum Efficiencies in Mn^{2+}-Doped $CsPbCl_3$ Perovskite Nanocrystals with Varied Dopant Concentration. *Chem. Mater.* **2017**, *29*, 8003−8011.
(20) Liu, X.; Xu, X.; Li, B.; Yang, L.; Li, Q.; Jiang, H.; Xu, D. Tunable Dual-Emission in Monodispersed Sb^{3+} /Mn^{2+} Codoped $Cs_2NaInCl_6$ Perovskite Nanocrystals through an Energy Transfer Process. *Small* **2020**, *16*, 2002547.
(21) Sihn, M. R.; Kirakosyan, A.; Jeon, M.-G.; Choi, J. Suppressed Mn^{2+} Doping in Organometal Halide Perovskite Nanocrystals by Formation of Two-Dimensional $(CH_3NH_3)_2MnCl_4$. *Chem. Commun.* **2021**, *57*, 5055−5058.
(22) Ke, B.; Zeng, R.; Zhao, Z.; Wei, Q.; Xue, X.; Bai, K.; Cai, C.; Zhou, W.; Xia, Z.; Zou, B. Homo- and Heterovalent Doping-Mediated Self-Trapped Exciton Emission and Energy Transfer in Mn-Doped $Cs_2Na_{1-x}Ag_xBiCl_6$ Double Perovskites. *J. Phys. Chem. Lett.* **2020**, *11*, 340−348.
(23) Majher, J. D.; Gray, M. B.; Strom, T. A.; Woodward, P. M. $Cs_2NaBiCl_6$:Mn^{2+} —A New Orange-Red Halide Double Perovskite Phosphor. *Chem. Mater.* **2019**, *31*, 1738−1744.
(24) Pinchetti, V.; Anand, A.; Akkerman, Q. A.; Sciacca, D.; Lorenzon, M.; Meinardi, F.; Fanciulli, M.; Manna, L.; Brovelli, S. Trap-Mediated Two-Step Sensitization of Manganese Dopants in Perovskite Nanocrystals. *ACS Energy Lett.* **2019**, *4*, 85−93.
(25) Luo, B.; Guo, Y.; Li, X.; Xiao, Y.; Huang, X.; Zhang, J. Z. Efficient Trap-Mediated Mn2+ Dopant Emission in Two Dimensional Single-Layered Perovskite (CH3CH2NH3)2PbBr4. *J. Phys. Chem. C* **2019**, *123*, 14239−14245.
(26) Rachna; Singh, A.; Lamba, R. S.; Kumar, S.; Sapra, S. Self-Trapped Excitons Mediated Energy Transfer to Sm^{3+}in $Cs_2AgIn_{(1-x)}Sm_xCl_6$:Bi Double Perovskite Nanocrystals. *J. Phys. Chem. C* **2023**, *127*, 468−475.
(27) Sheikh, T.; Nag, A. Mn Doping in Centimeter-Sized Layered 2D Butylammonium Lead Bromide (BA_2PbBr_4) Single Crystals and Their Optical Properties. *J. Phys. Chem. C* **2019**, *123*, 9420−9427.
(28) Das Adhikari, S.; Guria, A. K.; Pradhan, N. Insights of Doping and the Photoluminescence Properties of Mn-Doped Perovskite Nanocrystals. *J. Phys. Chem. Lett.* **2019**, *10*, 2250−2257.
(29) Shannon, R. D. Revised Effective Ionic Radii and Systematic Studies of Interatomie Distances in Halides and Chaleogenides. *Acta Crystallogr. Sect. A Found. Adv.* **1976**, *32*, 751−767.
(30) Mir, W. J.; Jagadeeswararao, M.; Das, S.; Nag, A. Colloidal Mn-Doped Cesium Lead Halide Perovskite Nanoplatelets. *ACS Energy Lett.* **2017**, *2*, 537−543.
(31) Liu, W.; Lin, Q.; Li, H.; Wu, K.; Robel, I.; Pietryga, J. M.; Klimov, V. I. Mn^{2+} -Doped Lead Halide Perovskite Nanocrystals with Dual-Color Emission Controlled by Halide Content. *J. Am. Chem. Soc.* **2016**, *138*, 14954−14961.
(32) Acharyya, P.; Maji, K.; Kundu, K.; Biswas, K. 2D Nanoplates and Scaled-Up Bulk Polycrystals of Ruddlesden−Popper $Cs_2PbI_2Cl_2$ for Optoelectronic Applications. *ACS Appl. Nano Mater.* **2020**, *3*, 877−886.
(33) Biswas, A.; Bakthavatsalam, R.; Kundu, J. Efficient Exciton to Dopant Energy Transfer in Mn^{2+} -Doped $(C_4H_9NH_3)_2PbBr_4$ Two-Dimensional (2D) Layered Perovskites. *Chem. Mater.* **2017**, *29*, 7816−7825.
(34) Su, B.; Molokeev, M. S.; Xia, Z. Unveiling Mn^{2+} Dopant States in Two-Dimensional Halide Perovskite toward Highly Efficient Photoluminescence. *J. Phys. Chem. Lett.* **2020**, *11*, 2510−2517.
(35) Dutta, A.; Behera, R. K.; Deb, S.; Baitalik, S.; Pradhan, N. Doping Mn(II) in All-Inorganic Ruddlesden−Popper Phase of Tetragonal $Cs_2PbCl_2I_2$ Perovskite Nanoplatelets. *J. Phys. Chem. Lett.* **2019**, *10*, 1954−1959.
(36) Dutta, S. K.; Dutta, A.; Das Adhikari, S.; Pradhan, N. Doping Mn^{2+} in Single-Crystalline Layered Perovskite Microcrystals. *ACS Energy Lett.* **2019**, *4*, 343−351.
(37) Ohya, S.; Ohno, K.; Tanaka, M. Magneto-Optical and Magnetotransport Properties of Heavily Mn-Doped GaMnAs. *Appl. Phys. Lett.* **2007**, *90*, 112503.
(38) Jadhav, P. A.; Panmand, R. P.; Patil, D. R.; Fouad, H.; Gosavi, S. W.; Kale, B. B. Triangular CdS Nanostructure: Effect of Mn Doping on Photoluminescence, Electron Spin Resonance, and Magneto-Optical Properties. *J. Nanoparticle Res.* **2017**, *19*, 218.
(39) Stroppa, A.; Picozzi, S.; Continenza, A.; Freeman, J. Electronic Structure and Ferromagnetism of Mn-Doped Group-IV Semiconductors. *Phys. Rev. B - Condens. Matter Mater. Phys.* **2003**, *68*, 1−9.
(40) Zeng, R.; Zhang, L.; Xue, Y.; Ke, B.; Zhao, Z.; Huang, D.; Wei, Q.; Zhou, W.; Zou, B. Highly Efficient Blue Emission from Self-Trapped Excitons in Stable Sb^{3+} -Doped $Cs_2NaInCl_6$ Double Perovskites. *J. Phys. Chem. Lett.* **2020**, *11*, 2053−2061.
(41) Lamba, R. S.; Basera, P.; Singh, S.; Bhattacharya, S.; Sapra, S. Lead-Free Alloyed Double-Perovskite Nanocrystals of $Cs_2(Na_xAg_{1-x})$-$BiBr_6$ with Tunable Band Gap. *J. Phys. Chem. C* **2021**, *125*, 1954−1962.
(42) Lamba, R. S.; Basera, P.; Bhattacharya, S.; Sapra, S. Band Gap Engineering in $Cs_2(Na_xAg_{1-x})BiCl_6$ Double Perovskite Nanocrystals. *J. Phys. Chem. Lett.* **2019**, *10*, 5173−5181.
(43) Torma, A. J.; Li, W.; Zhang, H.; Tu, Q.; Klepov, V. V.; Brennan, M. C.; McCleese, C. L.; Krzyaniak, M. D.; Wasielewski, M. R.; Katan, C.; et al. Interstitial Nature of Mn^{2+} Doping in 2D Perovskites. *ACS Nano* **2021**, *15*, 20550−20561.
(44) Yang, S.; Liang, Q.; Wu, H.; Pi, J.; Wang, Z.; Luo, Y.; Liu, Y.; Long, Z.; Zhou, D.; Wen, Y.; et al. Lead-Free Double Perovskite $Cs_2NaErCl_6$: Li^+ as High-Stability Anodes for Li-Ion Batteries. *J. Phys. Chem. Lett.* **2022**, *13*, 4981−4987.
(45) Ren, L.; Wang, Y.; Wang, M.; Wang, S.; Zhao, Y.; Cazorla, C.; Chen, C.; Wu, T.; Jin, K. Tuning Magnetism and Photocurrent in Mn-Doped Organic-Inorganic Perovskites. *J. Phys. Chem. Lett.* **2020**, *11*, 2577−2584.
(46) Han, P.; Zhang, X.; Luo, C.; Zhou, W.; Yang, S.; Zhao, J.; Deng, W.; Han, K. Manganese-Doped, Lead-Free Double Perovskite Nanocrystals for Bright Orange-Red Emission. *ACS Cent. Sci.* **2020**, *6*, 566−572.
(47) Chin, R. L.; Hercules, D. M. Surface Spectroscopic Characterization of Cobalt-Alumina Catalysts. *J. Phys. Chem.* **1982**, *86*, 360−367.
(48) Nelson, A. J.; Reynolds, J. G.; Roos, J. W. Core-Level Satellites and Outer Core-Level Multiplet Splitting in Mn Model Compounds. *J. Vac. Sci. Technol. A Vacuum, Surfaces, Film* **2000**, *18*, 1072−1076.
(49) Wang, S.; Shen, X.; Zhang, Y.; Zhuang, X.; Xue, D.; Zhang, X.; Wu, J.; Zhu, J.; Shi, Z.; Kershaw, S. V.; et al. Oxalic Acid Enabled Emission Enhancement and Continuous Extraction of Chloride from Cesium Lead Chloride/Bromide Perovskite Nanocrystals. *Small* **2019**, *15*, 1901828.
(50) Zhang, J.; Liu, X.; Jiang, P.; Chen, H.; Wang, Y.; Ma, J.; Zhang, R.; Yang, F.; Wang, M.; Zhang, J.; et al. Red-Emitting $CsPbBrI_2$/PbSe Heterojunction Nanocrystals with High Luminescent Efficiency and Stability for Bright Light-Emitting Diodes. *Nano Energy* **2019**, *66*, 104142.
(51) Kubelka, P.; Munk, F. An Article on Optics of Paint Layers. *Z. Technol. Phys.* **1931**, *12*, 593−601.
(52) Saleh, M. A.; Nugroho, A. A.; Dewi, K. K.; Supandi, A. R.; Onggo, D.; Kuhn, H.; van Loosdrecht, P. H. M. Optical Absorption Spectra of Mn^{2+} in of $(C_6H_5CH_2CH_2NH_3)_2$-$MnCl_4$ and

https://doi.org/10.1021/acs.jpcc.2c08506
J. Phys. Chem. C 2023, 127, 3609−3618

$(NH_2CH_2CH_2NH_2)_2$-$MnCl_4$ Hybrid Comp. *Key Eng. Mater.* **2019**, *811*, 179−183.
(53) Kahmann, S.; Tekelenburg, E. K.; Duim, H.; Kamminga, M. E.; Loi, M. A. Extrinsic Nature of the Broad Photoluminescence in Lead Iodide-Based Ruddlesden−Popper Perovskites. *Nat. Commun.* **2020**, *11*, 2344.
(54) Liang, M.; Lin, W.; Zhao, Q.; Zou, X.; Lan, Z.; Meng, J.; Shi, Q.; Castelli, I. E.; Canton, S. E.; Pullerits, T.; et al. Free Carriers versus Self-Trapped Excitons at Different Facets of Ruddlesden-Popper Two-Dimensional Lead Halide Perovskite Single Crystals. *J. Phys. Chem. Lett.* **2021**, *12*, 4965−4971.
(55) Rossi, D.; Parobek, D.; Dong, Y.; Son, D. H. Dynamics of Exciton−Mn Energy Transfer in Mn-Doped $CsPbCl_3$ Perovskite Nanocrystals. *J. Phys. Chem. C* **2017**, *121*, 17143−17149.
(56) Yuan, X.; Ji, S.; De Siena, M. C.; Fei, L.; Zhao, Z.; Wang, Y.; Li, H.; Zhao, J.; Gamelin, D. R. Photoluminescence Temperature Dependence, Dynamics, and Quantum Efficiencies in Mn^{2+} -Doped $CsPbCl_3$ Perovskite Nanocrystals with Varied Dopant Concentration. *Chem. Mater.* **2017**, *29*, 8003−8011.
(57) Cao, S.; Zheng, J.; Zhao, J.; Wang, L.; Gao, F.; Wei, G.; Zeng, R.; Tian, L.; Yang, W. Highly Efficient and Well-Resolved Mn^{2+} Ion Emission in MnS/ZnS/CdS Quantum Dots. *J. Mater. Chem. C* **2013**, *1*, 2540.
(58) Zhang, J.-C.; Zhao, L.-Z.; Long, Y.-Z.; Zhang, H.-D.; Sun, B.; Han, W.-P.; Yan, X.; Wang, X. Color Manipulation of Intense Multiluminescence from CaZnOS:Mn^{2+} by Mn^{2+} Concentration Effect. *Chem. Mater.* **2015**, *27*, 7481−7489.
(59) Foster, J. J.; Gill, N. S. Complex Halides of the Transition Metals. Part III. Electronic Spectra and Ligand Field Parameters of Octahedral and Tetrahedral Halogeno-Complexes of Manganese(II). *J. Chem. Soc. A Inorganic, Phys. Theor.* **1968**, 2625−2629.
(60) Luo, B.; Guo, Y.; Li, X.; Xiao, Y.; Huang, X.; Zhang, J. Z. Efficient Trap-Mediated Mn^{2+} Dopant Emission in Two Dimensional Single-Layered Perovskite $(CH_3CH_2NH_3)_2PbBr_4$. *J. Phys. Chem. C* **2019**, *123*, 14239−14245.
(61) Zhu, X.; Meng, S.; Zhao, Y.; Zhang, S.; Zhang, J.; Yin, C.; Ye, S. Mn^{2+}−Mn^{2+} Magnetic Coupling Effect on Photoluminescence Revealed by Photomagnetism in $CsMnCl_3$. *J. Phys. Chem. Lett.* **2020**, *11*, 9587−9595.
(62) De, A.; Mondal, N.; Samanta, A. Luminescence Tuning and Exciton Dynamics of Mn-Doped $CsPbCl_3$ Nanocrystals. *Nanoscale* **2017**, *9*, 16722−16727.
(63) Gonzalez Beermann, P. A.; McGarvey, B. R.; Muralidharan, S.; Sung, R. C. W. EPR Spectra of Mn^{2+} -Doped ZnS Quantum Dots. *Chem. Mater.* **2004**, *16*, 915−918.
(64) Yang, X.; Pu, C.; Qin, H.; Liu, S.; Xu, Z.; Peng, X. Temperature- and Mn^{2+} Concentration-Dependent Emission Properties of Mn^{2+} -Doped ZnSe Nanocrystals. *J. Am. Chem. Soc.* **2019**, *141*, 2288−2298.
(65) Pathak, N.; Gupta, S. K.; Ghosh, P. S.; Arya, A.; Natarajan, V.; Kadam, R. M. Probing Local Site Environments and Distribution of Manganese in $SrZrO_3$:Mn; PL and EPR Spectroscopy Complimented by DFT Calculations. *RSC Adv.* **2015**, *5*, 17501−17513.
(66) Liu, Y.; Zhang, J.; Han, B.; Wang, X.; Wang, Z.; Xue, C.; Bian, G.; Hu, D.; Zhou, R.; Li, D.-S.; et al. New Insights into Mn−Mn Coupling Interaction-Directed Photoluminescence Quenching Mechanism in Mn^{2+}-Doped Semiconductors. *J. Am. Chem. Soc.* **2020**, *142*, 6649−6660.
(67) Vink, A. P.; de Bruin, M. A.; Roke, S.; Peijzel, P. S.; Meijerink, A. Luminescence of Exchange Coupled Pairs of Transition Metal Ions. *J. Electrochem. Soc.* **2001**, *148*, E313.
(68) Su, J.; Han, Y.; Meng, S.; Yang, X.; Ye, S.; Zhang, Q. Tuning the Decay of Mn^{2+} Emission via Magnetically Coupling with Cr^{3+} in $ZnGa_2O_4$. *J. Appl. Phys.* **2018**, *124*, No. 063108.
(69) Lin, J.; Zhang, Q.; Wang, L.; Liu, X.; Yan, W.; Wu, T.; Bu, X.; Feng, P. Atomically Precise Doping of Monomanganese Ion into Coreless Supertetrahedral Chalcogenide Nanocluster Inducing Unusual Red Shift in Mn^{2+} Emission. *J. Am. Chem. Soc.* **2014**, *136*, 4769−4779.
(70) Chen, L.; Yang, W.; Fu, H.; Liu, W.; Shao, G.; Tang, B.; Zheng, J. Materials Mn^{2+} -Doped $Cs_2NaInCl_6$ Double Perovskites and Their Photoluminescence Properties. *J. Mater. Sci.* **2021**, *56*, 8048−8059.
(71) Locardi, F.; Cirignano, M.; Baranov, D.; Dang, Z.; Prato, M.; Drago, F.; Ferretti, M.; Pinchetti, V.; Fanciulli, M.; Brovelli, S.; et al. Colloidal Synthesis of Double Perovskite $Cs_2AgInCl_6$and Mn-Doped $Cs_2AgInCl_6$ Nanocrystals. *J. Am. Chem. Soc.* **2018**, *140*, 12989−12995.
(72) Zhou, G.; Su, B.; Huang, J.; Zhang, Q.; Xia, Z. Broad-Band Emission in Metal Halide Perovskites: Mechanism, Materials, and Applications. *Mater. Sci. Eng. R Reports* **2020**, *141*, 100548.
(73) Su, B.; Zhou, G.; Huang, J.; Song, E.; Nag, A.; Xia, Z. Mn2+-Doped Metal Halide Perovskites: Structure, Photoluminescence, and Application. *Laser Photonics Rev.* **2021**, *15*, 2000334.
(74) Zhou, G.; Jiang, X.; Molokeev, M.; Lin, Z.; Zhao, J.; Wang, J.; Xia, Z. Optically Modulated Ultra-Broad-Band Warm White Emission in Mn^{2+}-Doped $(C_6H_{18}N_2O_2)PbBr_4$ Hybrid Metal Halide Phosphor. *Chem. Mater.* **2019**, *31*, 5788−5795.
(75) Zhou, G.; Guo, S.; Zhao, J.; Molokeev, M.; Liu, Q.; Zhang, J.; Xia, Z. Unraveling the Mechanochemical Synthesis and Luminescence in Mn II -Based Two-Dimensional Hybrid Perovskite $(C_4H_9NH_3)_2PbCl_4$. *Sci. China Mater.* **2019**, *62*, 1013−1022.
(76) K, N. N.; Nag, A. Synthesis and Luminescence of Mn-Doped $Cs_2AgInCl_6$ Double Perovskites. *Chem. Commun.* **2018**, *54*, 5205−5208.
(77) Buonsanti, R.; Milliron, D. J. Chemistry of Doped Colloidal Nanocrystals. *Chem. Mater.* **2013**, *25*, 1305−1317.
(78) Guria, A. K.; Dutta, S. K.; Adhikari, S. D.; Pradhan, N. Doping Mn^{2+} in Lead Halide Perovskite Nanocrystals: Successes and Challenges. *ACS Energy Lett.* **2017**, *2*, 1014−1021.
(79) Sapra, S.; Prakash, A.; Ghangrekar, A.; Periasamy, N.; Sarma, D. D. Emission Properties of Manganese-Doped ZnS Nanocrystals. *J. Phys. Chem. B* **2005**, *109*, 1663−1668.
(80) Sapra, S.; Sarma, D. D.; Sanvito, S.; Hill, N. A. Influence of Quantum Confinement on the Electronic and Magnetic Properties of (Ga,Mn)As Diluted Magnetic Semiconductor. *Nano Lett.* **2002**, *2*, 605−608.
(81) Vargas, B.; Reyes-Castillo, D. T.; Coutino-Gonzalez, E.; Sánchez-Aké, C.; Ramos, C.; Falcony, C.; Solis-Ibarra, D. Enhanced Luminescence and Mechanistic Studies on Layered Double-Perovskite Phosphors: $Cs_4Cd_{1-x}Mn_xBi_2Cl_{12}$. *Chem. Mater.* **2020**, *32*, 9307−9315.
(82) Gill, D.; Bhumla, P.; Kumar, M.; Bhattacharya, S. High-Throughput Screening to Modulate Electronic and Optical Properties of Alloyed $Cs_2AgBiCl_6$ for Enhanced Solar Cell Efficiency. *J. Phys. Mater.* **2021**, *4*, No. 025005.
(83) Gill, D.; Singh, A.; Jain, M.; Bhattacharya, S. Exploring Exciton and Polaron Dominated Photophysical Phenomena in Ruddlesden−Popper Phases of $Ba_{N+1}Zr_nS_{3n+1}$ (n = 1−3) from Many Body Perturbation Theory. *J. Phys. Chem. Lett.* **2021**, *12*, 6698−6706.
(84) Basera, P.; Saini, S.; Bhattacharya, S. Self Energy and Excitonic Effect in (Un)Doped TiO_2 Anatase: A Comparative Study of Hybrid DFT, GW and BSE to Explore Optical Properties. *J. Mater. Chem. C* **2019**, *7*, 14284−14293.

https://doi.org/10.1021/acs.jpcc.2c08506
J. Phys. Chem. C 2023, 127, 3609−3618